Localization, Transport and Topological issues in certain Low Dimensional Lattices

The research work is submitted by

Sougata Biswas

Department of physics

Presidency University, Kolkata

Enrollment ID: PU/PHD/PHYS/2021/048

Registration No: R-21RS209170329

under the guidance of

Prof. Arunava Chakrabarti

Department of physics, Presidency University, Kolkata

1 Introduction

Our research mainly focuses on the electronic properties of certain low-dimensional lattices, specifically a recently developed class of geometrically decorated lattices with tailor-made structures.

We use a tight-binding formalism to study the localization-delocalization of single-particle states, transport properties, and later the problem of topological phase transitions in such decorated lattices. We have examined periodic, quasi-periodic, and fractal lattices. These artificial quantum lattice models have drawn a lot of attention lately because of their unique properties concerning topological and localization-delocalization issues, and because of the fact that improved lithographic and grafting tecniques have recently made such lattices a reality.

Just to give a glimpse of our achievements, we may begin with the Sierpinski gasket fractal (SGF) lattice where we could analytically unravel groups of compact localized states. We demonstrate that, these states are part of non-dispersive, flat energy bands when the SGF clusters are arranged in a periodic array. When the fractal substrate is enlarged to its thermodynamic limit, an infinite number of such compact localized states are extracted using a real space renormalization group technique. Thus, in our opinion, the scale-invariant SGF network makes an interesting substrate for a designer lattice.

In another work we investigate the paradoxical problem of a complete delocalization of all the single-particle eigenstates, for example, of an electron propagating in a medium with structured disorder. This work reveals results that are significantly richer than those that were previously known, such as the delocalization at unique energy eigenvalues in lattices with disorder that is geometrically correlated or in a class of low dimensional quasicrystalline lattices.

We also investigate the quantum dynamics of a wave packet on a particular class of one-dimensional quasiperiodic lattices. The mean square displacement, the temporal autocorrelation function, time dependence of the inverse participation ratio, and the information entropy — all of the so-called hallmarks of studying localization based on dynamics. The results indicate a complete turnover in the nature of the single particle states and the character of the energy spectrum under the appropriate circumstances.

In the final part of the thesis we address, using a lattice model, some issues related to the topological phase transition in polymer-like geometries. For this purpose, we have extended the popular Su-Scrieffer-Heeger (SSH) model. We have investigated the effects of the hopping amplitudes added to the model on its topological characteristics in detail. The robustness of edge states against disorder in various SSH mesh geometries has been discussed in details.

2 Outlines of my research works

This section will discuss some of our research works during my Ph.D. studies.

2.1 Designer quantum states on a fractal substrate: compact localization, flat bands, and the edge modes

Physica E 153 (2023) 115762

Contents lists available at ScienceDirect

Physica E: Low-dimensional Systems and Nanostructures

journal homepage: www.elsevier.com/locate/physe

Check for updates

Designer quantum states on a fractal substrate: Compact localization, flat bands and the edge modes

Sougata Biswas *, Arunava Chakrabarti

Department of Physics, Presidency University, 86/1 College Street, Kolkata, West Bengal 700 073, India

Artificially tailored lattice models of quantum networks that display translational invariance have recently garnered significant interest from the condensed matter physics community. In such lattices, the local environment surrounding a site or a cluster of sites triggers destructive quantum interference, which leads to the occurrence of non-dispersive, flat Bloch bands. The group velocity of an excitation occupying a flat band (FB) becomes zero, resulting in an infinitely large effective mass of the excitation. Wave propagation is thereby inhibited.

A disorder in the system is not necessary for such a localization of waves. In a system that displays flat bands (FBs), the wavefunction's amplitude is usually non-zero over a group of sites, or what we might refer to as an "island", that is isolated from another such island by sites on which theamplitudes of the wavefunction are zero. These states are known as compact localized states (CLS). Since it is now possible to precisely engineer an excitation's wave function in networks on an atomic scale, the CLS's have drawn a lot of attention lately. The development of well-defined quantum nanostructures through atom-by-atom manipulation and the immense atomic-scale tunability is creating enormous opportunities for investigating not only the fundamental physics of the quantum world but also the potential of these designer states in transmitting quantum information [1, 2, 3, 4, 5].

We unravel and analyze analytically compact localized single-particle eigenstates on a deterministic fractal substrate, represented by a triangular Sierpinski gasket of arbitrarily large size. We prescribe an exact real space renormalization group (RSRG) decimation scheme within a tight binding formalism to discern these states and argue that the number of such states can be infinite if the fractal substrate is enlarged to its thermodynamic limit.

We revisit the SGF in the light of the designer quantum states, which will form the CLS on such a fractal substrate. The recursive growth of an SGF pattern with an inherent self-similarity naturally invites an implementation of a real space renormalization group (RSRG) decimation method [6], which we will eventually explore. First of all we elucidate the strength of the RSRG decimation scheme to obtain the dispersion relations for three variants of a sawtooth chain, and obtain the $E-k$ diagrams. In the first example, that of a simple array of triangles, our results exactly match the existing results obtained through a direct diagonalization of the Hamiltonian in k-space. The next example is an extended version of a basic sawtooth lattice, unaddressed so

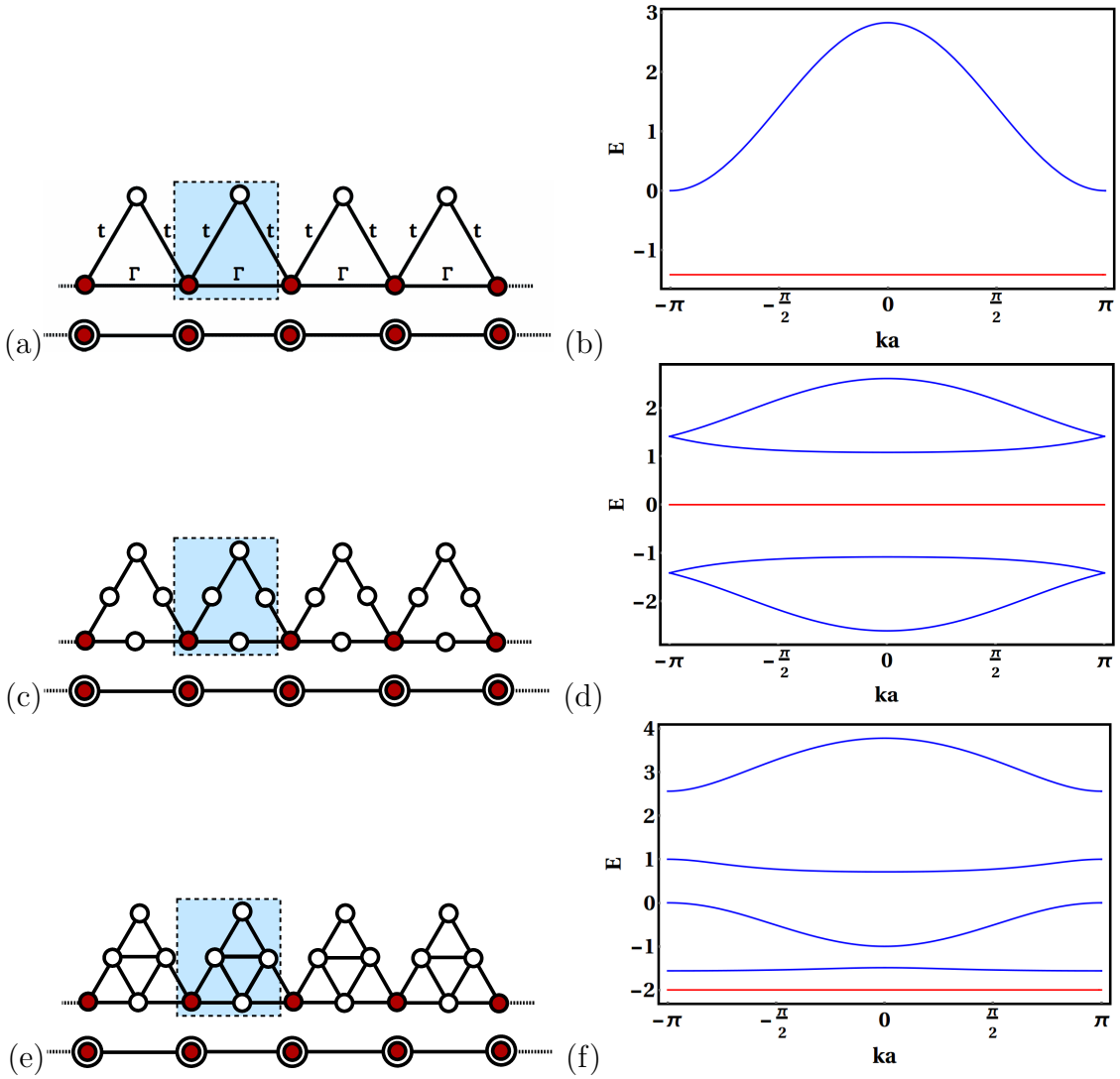

Figure 1: (Color online) (a) A simple periodic sawtooth array with two different types of hopping integrals Γ and t, (c) a periodic triangular array with one extra atomic site in each arm, and with a uniform hopping t, and (e) a periodic array of the G_1 Sierpinski gasket network with uniform hopping t along each arm. Corresponding Energy-wave vector dispersion relations are shown with $\epsilon = 0$, $t = 1$, $\Gamma = 1/\sqrt{2}$ in (b), and with $\epsilon = 0$ and $t = 1$ in (d) and (f) respectively. Flat bands are drawn in red. The flat bands energies are, (b) $E = -\sqrt{2}$ (non degenerate), (d) $E = 0$ (non degenerate), (f)$E = -2$ (non degenerate).

far, to the best of our knowledge, and the third example discusses a periodic array of the first generation SGF palquette, acting as the 'unit cell'. In each case, a flat, non-dispersive energy band is seen to exist which corresponds to a CLS in the basic isolated cluster. The design of such CLS will be discussed in details, in respect of an SGF. Subsequently, the RSRG method will be used efficiently to construct the CLS on an SGF of any arbitrarily large generation and to exactly evaluate the corresponding energy eigenvalues.

Secondly, we construct periodic chains in one dimension by repeating unit cells that are SGF's with sequentially increasing generations. We use a decimation scheme to map the structure onto a purely one dimensional geometry with energy dependent on-site potentials and the hopping integrals, and find that the $E - k$ spectrum displays both the dispersive and non-dispersive energy bands that get more and more densely packed as the structural motif contains higher and higher generation SGF units. The flat, non-dispersive bands occur exactly at the same energy eigenvalues for which the CLS are formed on the corresponding finite generation

SGF substrate. A plethora of such CLS evolves as the SGF motif grows in size.

We refer to Fig. 1, where a basic sawtooth array (BSA)(in (a)), a sawtooth superlattice (SSL) with just an extra atomic site on each side of the triangle (in (c)) and an SGF-sawtooth (SGFS) array with a first generation SGF embedded inside the triangle (in (e)) are shown. The 'unit cell' for each lattice is shown in blue shade.

We consider spinless, non-interacting fermions on all these (and subsequent ones in other sections) systems and use the tight-binding Hamiltonian,

$$H = \epsilon \left|i\right\rangle \left\langle i\right| + \sum_{<ij>} \tau_{ij} \left|i\right\rangle \left\langle j\right| + h.c. \tag{1}$$

ϵ is the on-site potential (assumed constant), and τ_{ij} symbolizes the nearest neighbor hopping integral. For Fig. 1(a) τ_{ij} is chosen to have two different values, viz, t and Γ corresponding to the particle's 'hop' along the slanting arms and the horizontal arm of the triangle respectively.

Using the set of difference equations,

$$(E - \epsilon)\psi_i = \sum_j \tau_{ij}\psi_j \tag{2}$$

with j representing the nearest neighbor sites of i, we decimate every 'top' vertex (unfilled circle) in the BSA, shown in Fig. 1(a), and retain the 'base' atoms (red colored), which are now 'renormalized' and lie on an effective one-dimensional chain. The renormalized chain has an effective, energy-dependent on-site potential, and an energy-dependent nearest neighbor hopping integral, given by,

$$\begin{aligned} \tilde{\epsilon} &= \epsilon + \frac{2t^2}{E - \epsilon} \\ \tilde{t} &= \Gamma + \frac{t^2}{E - \epsilon} \end{aligned} \tag{3}$$

The dispersion relation for the effective 1-d chain can then easily be written down as,

$$E = \tilde{\epsilon} + 2\tilde{t}\cos\ ka \tag{4}$$

that expands, with a choice of $\Gamma = t/\sqrt{2}$,

$$\left[E - (\epsilon - \sqrt{2}t)\right]\left[E - \epsilon - 2\sqrt{2}t\cos^2(ka/2)\right] = 0 \tag{5}$$

Here, a is the effective lattice constant on the 1-d chain. Eq. (5) clearly shows a FB at $E = \epsilon - \sqrt{2}t$ that matches exactly with $E = \mp\sqrt{2}$ for $\epsilon = 0$ and $t = \pm 1$. The bands are shown in Fig. 1(b). Fig. 1(c) shows an extension of the sawtooth geometry, an SSL. The presence of an additional atom in each arm now results in a richer band spectrum (Fig. 1(d)) showing a flat band at the centre of the spectrum $E = \epsilon = 0$. The empty circles are decimated out, and the resulting 1-d chain has a dispersion relation,

$$(E - \epsilon)\left[1 - \left(\frac{4t^2\alpha + 2t^4 + 2(\alpha t^2 + t^4)\cos\ ka}{\delta}\right)\right] = 0 \tag{6}$$

Here, $\alpha = (E - \epsilon)^2 - 2t^2$, and $\delta = \alpha(E - \epsilon)^2$. The FB at $E = \epsilon$ is obvious.

In the SGFS, shown in Fig. 1(e), we depict a sawtooth array where a first-generation SGF replaces every basic triangle in Fig. 1(a). The decimation of the empty circles leads to the 1-d chain depicted immediately below the sawtooth array. The dispersion relation in this case is given by,

$$(E - \epsilon + 2t)\ \xi(E, k) = 0 \tag{7}$$

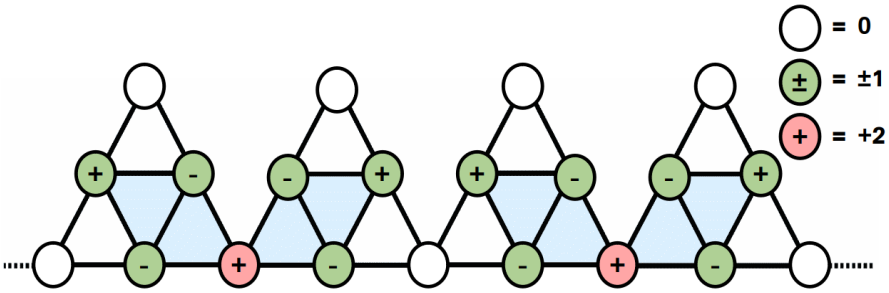

Figure 2: (Color online) Distribution of amplitudes on a first generation SGF array corresponding to the flat band energy $E = -2$ (non degenerate). The on-site potential for all the sites is set to zero, and the hopping integral is chosen as $t = 1$ along every arm of the gasket.

with $\xi(E,k) = (E-\epsilon)^5 - 4t(E-\epsilon)^4 - t^2(E-\epsilon)^3 + 12t^3(E-\epsilon)^2 - 2t^4(E-\epsilon) - 4t^5 - 2t^2[(E-\epsilon)^3 - t(E-\epsilon)^2 - 3t^2(E-\epsilon) + 2t^3]\cos\ ka$. The non-dispersive, FB is seen to appear at $E = \epsilon - 2t$ and is displayed in Fig. 1(f), along with the dispersive bands.

The distribution of the amplitudes of the wavefunction at an energy $E = \epsilon - 2t$ for this particular CLS on a G_1-SGF sawtooth array is shown in Fig. 2.

It is to be noted that, this particular CLS can not be drawn on an isolated SGF at its G_1 stage, owing to the geometrical frustration built in the network. It should be appreciated that, when a sawtooth-like array of finite-size gaskets are formed, the on-site potential ϵ_A of the 'top' vertex of the triangle renormalizes differently compared to the bulk sites having an on-site potential ϵ_B as one recursively uses the RSRG decimation scheme. We can make use of the RSRG recursion relations, that are already obtained earlier in the literature [6], viz,

$$\begin{aligned} \epsilon_{A,n} &= \epsilon_{A,n-1} + \frac{2t_{n-1}^2(E-\epsilon_{B,n-1})}{\Delta_{n-1}} \\ \epsilon_{B,n} &= \epsilon_{B,n-1} + \frac{4t_{n-1}^2(E-\epsilon_{B,n-1})}{\Delta_{n-1}} \\ t_n &= \frac{t_{n-1}^2(E-\epsilon_{B,n-1}+2t_{n-1})}{\Delta_{n-1}} \end{aligned} \tag{8}$$

where, $\Delta_{n-1} = (E-\epsilon_{B,n-1})(E-\epsilon_{B,n-1}-t_{n-1}) - 2t_{n-1}^2$, to accomplish the task of extracting the CLS (or equivalently, the FB) energy eigenvalues. Here, n denotes the number of times the RSRG decimation is implemented. Naturally, $n = 0$ implies the basic, un-renormalized gasket. The scheme is outlined below.

Following the same line of analysis, as discussed with reference to Fig. 1 (e), an SGF array comprising any large G_{n+1} motif as unit cell is reduced to an effective array of G_1 cells by renormalizing the SGF cluster n times. The dispersion relation for the linear chain of G_{n+1} SGF clusters is now given by the equation,

$$(E - \epsilon_{B,n} + 2t_n)\ \chi_n(E,k) = 0 \tag{9}$$

where,

$$\chi_n(E,k) = (E-\epsilon_{B,n})(E-\epsilon_{B,n}-3t_n) - \frac{4t_n^4(E-\epsilon_{B,n}+2t_n)}{\Lambda_n}\cos^2(ka/2) - 2t_n^2\cos\ ka \tag{10}$$

Here, $\Lambda_n = (E-\epsilon_{A,n})\Delta_n - 2t_n^2(E-\epsilon_{B,n})$. Clearly, the CLS on an isolated gasket, as well as the FB energy eigenvalues are extracted from the zero's of the polynomial equation

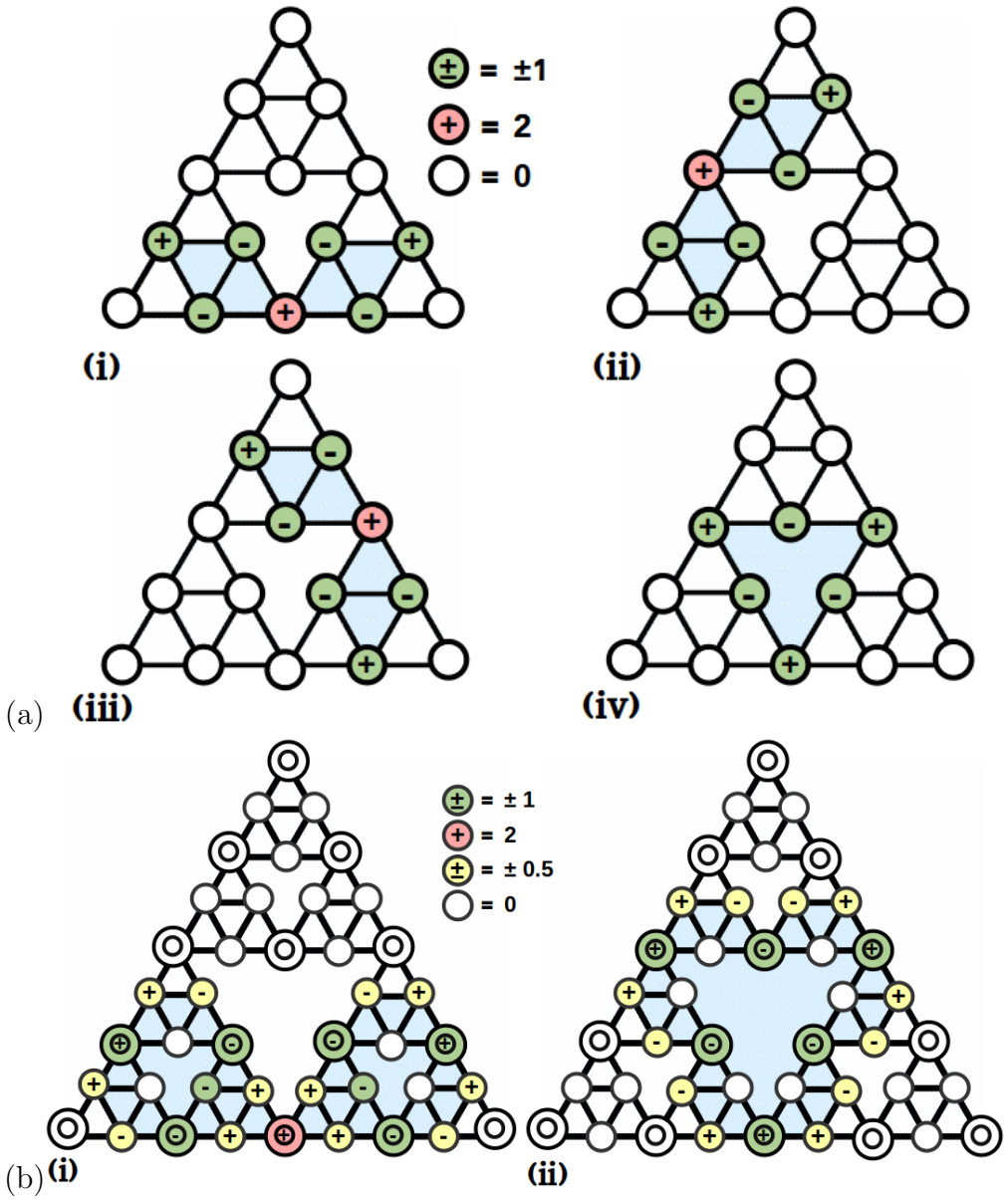

Figure 3: (Color online) (a) Distribution of compact localized amplitudes on a second generation (G_2) SGF network. The energy is $E = -2$ (four fold degenerate). The same energy and the same configuration of the amplitudes belong to a flat, non-dispersive band when we make a periodic array of G_2 units. Four different amplitude-distributions are shown in (i), (ii), (iii), (iv). (b) Distribution of the CLS amplitudes on the third generation (G_3) SGF. The compact localization is there corresponding to an energy eigenvalue $E = 1$. This also happens to be the flat band energy for an array of G_3 motifs. Only two different amplitude-distributions are shown in (i) and (ii). The on-site potential for all the sites is set to zero, and the uniform nearest neighbor hopping integral is chosen as $t = 1$.

$E - \epsilon_{B,n} + 2t_n = 0$, and the dispersive bands for the 'array' are obtained out of the equation $\chi_n(E, k) = 0$.

The recursion relations in Eq. 8 have the unique property of recurring roots, in the sense that the roots of the equation $E - \epsilon_{B,n} + 2t_n = 0$ are again found among the roots of the equation $E - \epsilon_{B,n+1} + 2t_{n+1} = 0$. Writing down explicitly, using Eq. (8), we find that the equation $E - \epsilon_{B,n+1} + 2t_{n+1} = 0$ simplifies to,

$$(E - \epsilon_{B,n} + 2t_n)\left[(E - \epsilon_{B,n})(E - \epsilon_{B,n} - 3t_n) + 2t_n^2\right] = 0 \tag{11}$$

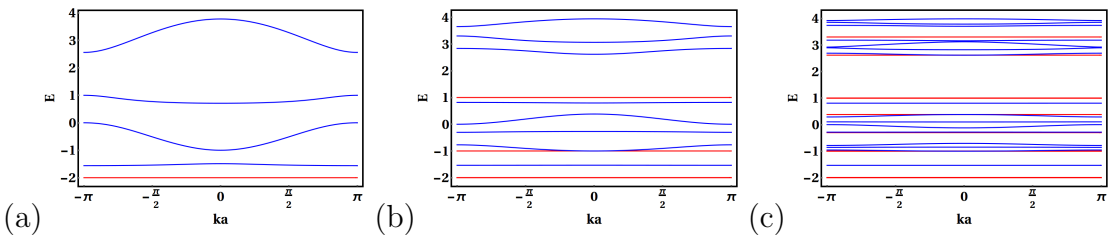

Figure 4: (Color online) Energy-wave vector (E - ka) dispersion relation of periodic arrays of (a) first, (b) second and (c) third generation Sierpinski gasket fractal (SGF) clusters as unit cells. We have chosen all onsite potentials $\epsilon = 0$ and hopping parameters $t = 1$. Flat bands are drawn in red.

The re-emergence of the roots at the n-th level in the $n+1$-th level is clear. Of course, there will be other roots as well, distinct from the previous ones.

In Fig. 3 we show how the amplitudes of the CLS wavefunctions are distributed among the sites of a finite size G_2 (in (a)) and G_3 (in (b)) SGF lattice. It should be quite clear now that, the same distributions will remain intact if we arrange such finite clusters periodically to design a decorated sawtooth chain of SGF's. Fig. 3(a) shows three equivalent amplitude distributions of the four-fold degenerate CLS at $E = -2$ in (i), (ii) and (iii). We have set $\epsilon_A = \epsilon_B = 0$ and $t = 1$. The distributions are rotated with respect to each other by an angle of $2\pi/3$. The fourth in the panel (a) shows another degenerate configuration where the amplitudes are pinned along the perimeter of the central blue shaded hexagon. This is kind of a *ring localized state*. As every 'void' built in the SGF makes the neighboring sites sitting actually on an edge, the state depicted in Fig. 3$a(iv)$ may easily be identified as an *edge state* in an SGF. In a sense, the three previous CLS distributions, occupying the vertices of the juxtaposed rhombii (shaded blue) also form a subset of the edge states, as the rhombii rest on any one of the sides (an edge again) of the full SGF cluster.

To explore the edge state configurations at a different energy eigenvalue, we go over to a 3rd generation (G_3) SGF unit cell, and work out a CLS amplitude distribution for $E = 1$, obtained as a solution of the equation $E - \epsilon_{B,1} + 2t_1 = 0$. The distribution is shown in panels (i) and (ii) of Fig. 3(b). It is to be observed that, even on this larger version of the gasket, the compactness of the states is preserved. The non-zero amplitudes now penetrate deeper into the bulk of the system, but the states retain their 'edge' or ring localization character at this scale of length.

To verify that the CLS states shown in Fig. 3 indeed belong to the FB's for an array of higher generation SGF motifs, in Fig. 4 we plot the dispersion curves of linear arrays of finite size SGF with G_1, G_2 and G_3 clusters as unit cells. The red colored lines mark the flat bands, and the corresponding energy eigenvalues turn out to be localized on a compact, finite subcluster of the SGF. The distribution is preserved even if the finite size of the gasket is arbitrarily large.

2.2 Complete escape from localization on a hierarchical lattice: A Koch fractal with all states extended

PHYSICAL REVIEW B **108**, 125430 (2023)

Complete escape from localization on a hierarchical lattice: A Koch fractal with all states extended

Sougata Biswas* and Arunava Chakrabarti†
Department of Physics, Presidency University, 86/1 College Street, Kolkata, West Bengal 700 073, India

(Received 25 July 2023; accepted 11 September 2023; published 25 September 2023)

In this research work, we investigate the counterintuitive case of a *complete delocalization* of all the single-particle states, representing, say, an electron propagating in a disordered environment, where the disorder has a *structure*. Delocalization of single-particle states in lattices with geometrically correlated disorder is not new, and began with the pioneering 'random dimer model' (RDM) [7, 8]. It was substantiated later by several other interesting works on (geometrically) correlated disordered lattices [9, 10, 11, 12, 13], and also in a whole class of quasiperiodic lattices where the *dimer-like* [7] geometric correlation is built in the growth sequences [14, 15, 16, 17, 18]. Delocalized eigenstates are also seen in deterministic fractal lattice models [20, 19, 21], and the origin of the existence of extended, delocalized single-particle states in such lattices can be traced back to the lattice geometry as a whole, in contrast to *local* clusters of sites, as shown in the RDM's or the quasiperiodic lattices referred to above.

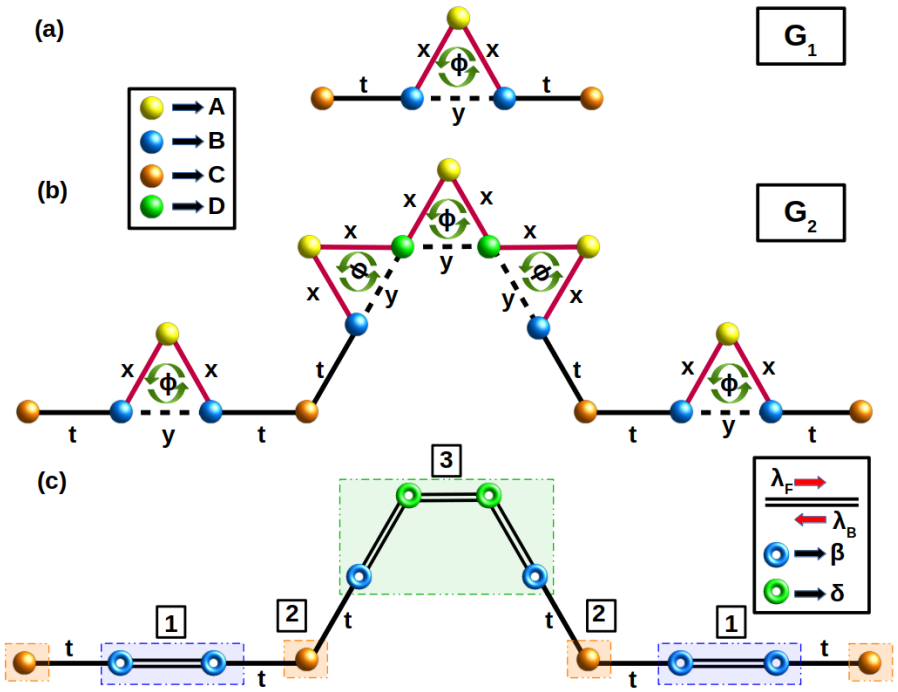

Figure 5: (Color online) (a) The building block (seed) of a Koch fractal. (b) The Koch fractal is in its second generation. The variety of sites A, B, C, and D are explained through the color code in the inset. (c) A linear chain is obtained from (b) after decimating out the A sites. The magnetic flux trapped in the triangular plaquettes, in each figure, is shown as Φ.

In all the previous works mentioned above, delocalization (leading to extended eigenfunctions) is observed only at special energy eigenvalue. In an infinitely large quasiperiodic lat-

tice [14, 15, 16] or in a deterministic fractal in its thermodynamic limit [19, 21], one can extract an infinity of such *resonant* energy eigenvalues leading to unscattered single-particle states. But, the distribution of such energy values is always of a discrete nature, and the energies do not really form a continuous band, and definitely do not span the entire spectrum of eigenvalues.

In the present work, we look deeper into this aspect of the problem, that is, we look into the possibility and the mechanism of generating an absolutely continuous band of energy eigenvalues with *all* states extended, in a disordered environment.

The KF geometry in this work (Fig. 5(a, b)) is described using a tight binding Hamiltonian with a distribution of the nearest neighbor hopping integrals. The four kinds of atomic sites (vertices) are distinguished depending on the number of the nearest neighbors. The colors are explained by the codes given in Fig. 5. There is a uniform magnetic field, piercing each triangle perpendicular to its plane. The field results in a magnetic flux Φ 'trapped' in every triangular plaquette [22]. This breaks the time-reversal symmetry only *locally*, that is when an electron circulates around the triangle.

The system is described using a tight binding Hamiltonian, viz,

$$H = \epsilon \left|i\right\rangle \left\langle i\right| + \sum_{<ij>} \tau_{ij} \left|i\right\rangle \left\langle j\right| + h.c. \tag{12}$$

The time-independent Schrödinger equation $H\psi = E\psi$ is cast into an equivalent set of discrete difference equations. The equations for the atomic sites at the vertices of a triangle read,

$$(E - \epsilon)\psi_i = \sum_j \tau_{ij}\psi_j \tag{13}$$

with $\tau_{ij} = t$, $x\exp(\pm i\theta_x)$, or $y\exp(\pm i\theta_y)$ as the case may be, and the sign of the Peierls' phase chosen appropriately. The summation runs over the nearest neighbors of the vertex considered.

Using Eqs. (13) we first decimate out [23] the A-sites (yellow colored) throughout the KF geometry, and map the entire lattice onto a purely one-dimensional chain (Fig. 5(c)).

$$\begin{aligned} \epsilon_\beta &= \epsilon + \frac{x^2}{(E-\epsilon)} \\ \epsilon_\delta &= \epsilon + \frac{2x^2}{(E-\epsilon)} \end{aligned} \tag{14}$$

Owing to the broken time-reversal symmetry caused by the trapped flux Φ, the *forward* (F) and *backward* (B) hopping integrals across such pairs are complex conjugates of each other. The 'forward' hopping integrals are given by, $t^F_{\beta\beta} = t^F_{\beta\delta} = t^F_{\delta\delta} = \lambda\exp(i\xi) \equiv \lambda_F$ (say), where,

$$\begin{aligned} \lambda &= \sqrt{y^2 + \frac{x^4}{(E-\epsilon)^2} + \frac{2x^2 y\cos(2\pi\Phi/\Phi_0)}{E-\epsilon}} \\ \xi &= \tan^{-1}\left[\frac{y\sin(\theta_y) - \frac{x^2\sin(2\theta_x)}{E-\epsilon}}{y\cos(\theta_y) + \frac{x^2\cos(2\theta_x)}{E-\epsilon}}\right] \end{aligned} \tag{15}$$

On the effectively linear chain (Fig. 5(c)) one can connect the amplitudes of the wave function on neighboring sites using transfer matrices.

$$(E - \epsilon_n)\psi_n = t_{n,n+1}\psi_{n+1} + t_{n,n-1}\psi_{n-1} \tag{16}$$

One can relate the amplitudes of the wave function ψ_n and $\psi_{n\pm1}$ through a matrix equation,

$$\begin{bmatrix} \psi_N \\ \psi_{N-1} \end{bmatrix} = \prod_{n=N-1}^{1} \mathcal{M}_n \begin{bmatrix} \psi_1 \\ \psi_0 \end{bmatrix} \tag{17}$$

$$\mathcal{M}_n = \begin{bmatrix} \frac{E-\epsilon_n}{t_{n,n+1}} & -\frac{t_{n,n-1}}{t_{n,n+1}} \\ 1 & 0 \end{bmatrix} \tag{18}$$

The string of matrices in the product $\prod_n \mathcal{M}_n$ corresponding to Fig. 5(c) now reads,

$$\prod_n \mathcal{M}_n = \mathcal{M}_2\mathcal{M}_1\mathcal{M}_2\mathcal{M}_3\mathcal{M}_2\mathcal{M}_1\mathcal{M}_2 \tag{19}$$

Let us work out the commutators $[\mathcal{M}_2, \mathcal{M}_1]$ and $[\mathcal{M}_2, \mathcal{M}_3]$. These turn out to be,

$$[\mathcal{M}_2, \mathcal{M}_{1(3)}] = \begin{bmatrix} 0 & \Gamma_{2,1(3)} \\ \Gamma_{2,1(3)} & 0 \end{bmatrix} \tag{20}$$

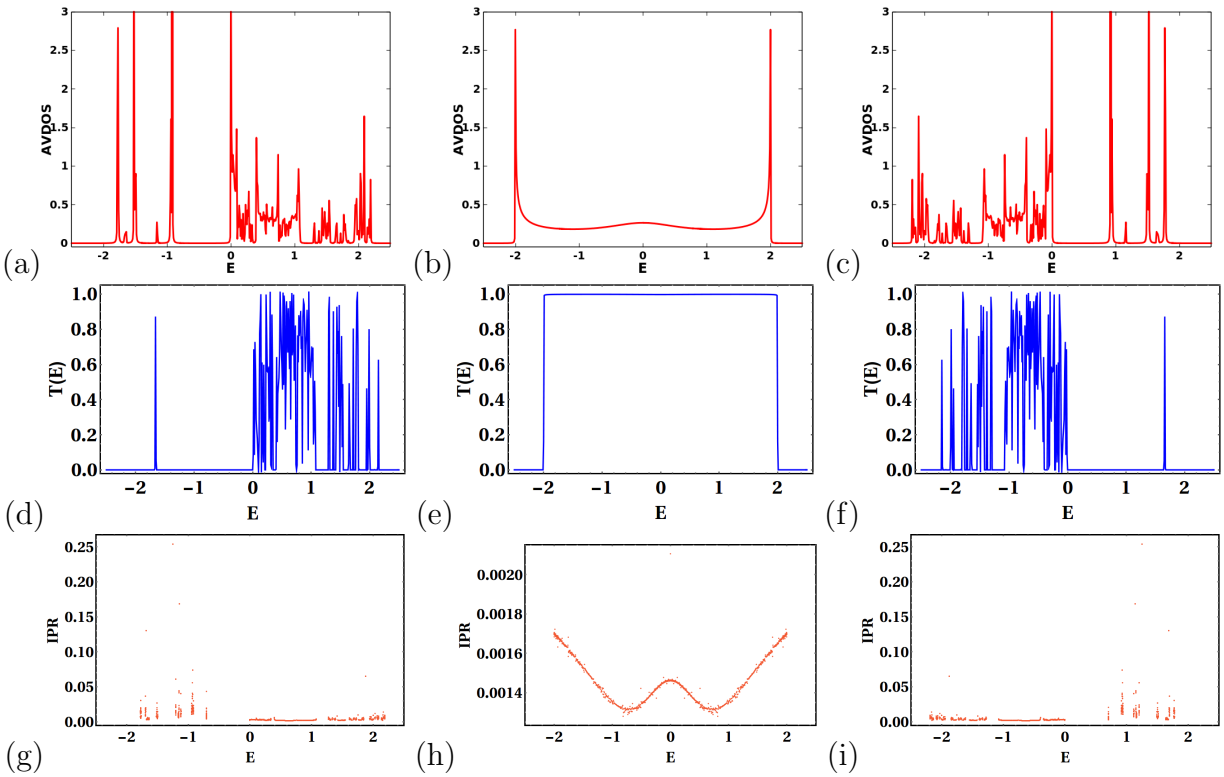

Figure 6: (Color online) (a) - (c) display the average density of states of an infinite Koch fractal, obtained using the decimation renormalization method outlined in appendix A. (d) - (f) depict the transmission co-efficient plotted against the energy, and (g) - (i) show the variation of the inverse participation ratio (IPR) with energy. The transmission coefficient and the IPR have been calculated for a Koch fractal in its 5th generation. The parameters, for all the figures, are chosen as, $\epsilon = 0$, $t = 1$, $x = y = \frac{1}{\sqrt{2}}$. The magnetic flux $\Phi = 0$ in (a),(d),(g), $\Phi = \frac{1}{4}\Phi_0$ in (b), (e), (h), and $\Phi = \frac{1}{2}\Phi_0$ in (c), (f), (i). Φ_0 has been set equal to unity.

where,

$$\Gamma_{2,1} = -\frac{e^{i\frac{4\pi\Phi}{3\Phi_0}}\left[2x^2y\cos\frac{2\pi\Phi}{\Phi_0}+(E-\epsilon)(-t^2+x^2+y^2)\right]}{t\left[x^2+e^{i\frac{2\pi\Phi}{\Phi_0}}(E-\epsilon)y\right]}$$

$$\Gamma_{2,3} = -\frac{e^{i\frac{4\pi\Phi}{\Phi_0}}\left[(E-\epsilon)(-t^2+x^2+y^2)+2x^2y\cos\frac{2\pi\Phi}{\Phi_0}\right]\xi}{t\left[x^2+e^{i\frac{2\pi\Phi}{\Phi_0}}(E-\epsilon)y\right]^3} \tag{21}$$

With, $\xi = E^4-4E^3\epsilon+6E^2\epsilon^2-4E\epsilon^3+\epsilon^4-4E^2x^2+8E\epsilon x^2-4\epsilon^2x^2+3x^4-(E-\epsilon)^2y^2-2(E-\epsilon)x^2y\cos\frac{2\pi\Phi}{\Phi_0}$. From Eqs. (20) and Eqs. (21), it is clear that a selection of $x^2+y^2=t^2$ and $\Phi=\frac{1}{4}\Phi_0$ makes $\left[\mathcal{M}_2,\mathcal{M}_{1(3)}\right]=0$ *independent of energy* E. This implies that, in the effectively linear chain in Fig. 5(c) and its longer versions (of any length actually), we can rearrange the clusters 1, 2, or 3 in *any* sequence. For example, we can switch their positions to form a *completely periodic* pattern.

The eigenvalue spectrum is conveniently captured in the average density of states (ADOS) of the system under study. Here, exploiting the self-similarity of the KF structure we have adopted a real space renormalization group (RSRG) method [24] to obtain the average density of states of an infinite KF. The ADOS is given by,

$$\rho(E) = w_A\rho_A(E)+w_B\rho_B(E)+w_C\rho_C(E)+w_D\rho_D(E) \tag{22}$$

where, ρ_J $(j=A,B,C,D)$ is the 'local' density of states at the site of type j, and the respective concentrations w_j $(j=A,B,C,D)$ are obtained as, $w_A=w_B=1/3$, and $w_C=w_D=1/6$.

In Fig. 6(a) - (c) we show the average density of states (AVDOS) of an infinite Koch fractal, obtained by the RSRG decimation scheme. Three prototype AVDOS profiles are shown. In Fig. 6(a) and (c) the AVDOS is shown when the flux threading each triangular plaquette are $\Phi=0$ and $\Phi=(1/2)\Phi_0$ respectively. The remarkable change in the AVDOS profile, brought out under the commutation condition $x^2+y^2=t^2$, and $\Phi=\Phi_0/4$, is explicitly seen in Fig. 6(b). It can be seen that, the fragmented AVDOS profiles in (a) or (c) now collapse into a single, *absolutely continuous* spread of energy eigenvalues E ranging between $[-2,2]$. We have examined numerous combinations of x and y, maintaining the condition $x^2+y^2=t^2$, and keeping the flux fixed at $\Phi=\Phi_0/4$. For any energy eigenvalue, picked up at random from anywhere within the energy spectrum in Fig. 6(b), and for *any combination* of the set (x,y), satisfying $x^2+y^2=t^2$, and with $\Phi=\Phi_0/4$, the numerical values of hopping integrals keep on oscillating, without showing any sign of convergence to zero. This implies that, for any energy within the band, there is a non-zero overlap between the wavefunctions at *all* scales of length. This is a confirmatory test for the extendedness of the wave function, a fact that is substantiated by the perfect two-terminal transport, as depicted in Fig. 6(e).

To strengthen the argument regarding the extended character of the eigenstates under the special condition referred to above, we have evaluated the inverse participation ratio (IPR) for increasingly larger finite-sized Koch fractal lattices. In Fig. 6 (g) - (i) one such case is shown, for three different flux values. The panel (g) for $\Phi=0$ and panel (i) for $\Phi=\Phi_0/2$, finite values of the IPR indicate the existence of localized eigenstates. However, as one enforces the resonance (commutation) condition, the gross IPR profile distinctly comes down arbitrarily close to zero, implying that a long enough Koch geometry, with $x^2+y^2=t^2$ and $\Phi=\Phi_0/4$, will support *only* extended wavefunctions.

2.3 Engineering complete delocalization of single particle states in a class of one dimensional aperiodic lattices: a quantum dynamical study

Physica E 162 (2024) 116010

Contents lists available at ScienceDirect

Physica E: Low-dimensional Systems and Nanostructures

journal homepage: www.elsevier.com/locate/physe

Engineering complete delocalization of single particle states in a class of one dimensional aperiodic lattices: A quantum dynamical study

Sougata Biswas *, Arunava Chakrabarti

Department of Physics, Presidency University, 86/1 College Street, Kolkata, West Bengal, 700 073, India

We undertake an in-depth study of the quantum dynamics [25, 26, 27] of a wave packet on a class of lattices that are essentially one dimensional in character with one or more atoms side-coupled to the backbone. Two such examples, based on a quasiperiodic Fibonacci lattice are discussed in details in this paper, and are shown in Fig. 7 (a) and (b). The analysis presented in the paper of course remains valid for any arrangement (placement) of the unit cells that build the lattice, be it quasiperiodic of any kind, or randomly disordered. The atoms, tunnel-coupled from the side are shown in red color. We work within a tight binding formalism and specifically intend to investigate the dynamics of the wave packet when the hopping (overlap) integrals in the Hamiltonian are numerically correlated in such a way that these non-translationally invariant systems have a continuous distribution of energy eigenvalue, and the wavefunctions turn out to be extended in character.

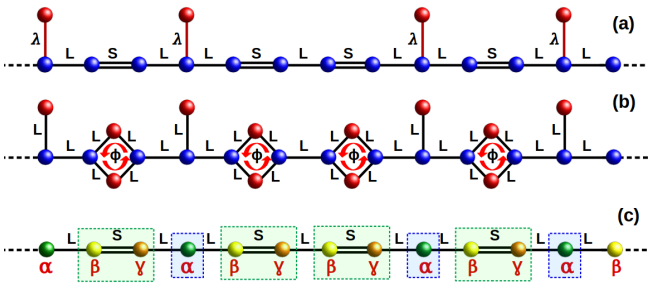

Figure 7: (Color online) The Fibonacci array of (a) 'dimer-stub' and (b) 'diamond-stub' quantum networks, where each diamond plaquette is threaded by a constant magnetic flux Φ. (c) The renormalized version of (a) and (b) is obtained after decimating the red-colored sites.

The tight binding Hamiltonian in Wannier basis, is written as,

$$H = \epsilon \left|n\right\rangle \left\langle n\right| + \sum_{<nm>} V_{nm} \left|n\right\rangle \left\langle m\right| + h.c. \tag{23}$$

Here, ϵ is the uniform on-site potential (set equal to zero in all our numerical calculations), and V_{nm} symbolizes the hopping amplitude between the nearest neighbors.

The wave packet of an electron at time $t = 0$ is written as,

$$\left|\Psi(0)\right\rangle = \sum_{n} C_n(0) \left|\psi_n(0)\right\rangle \tag{24}$$

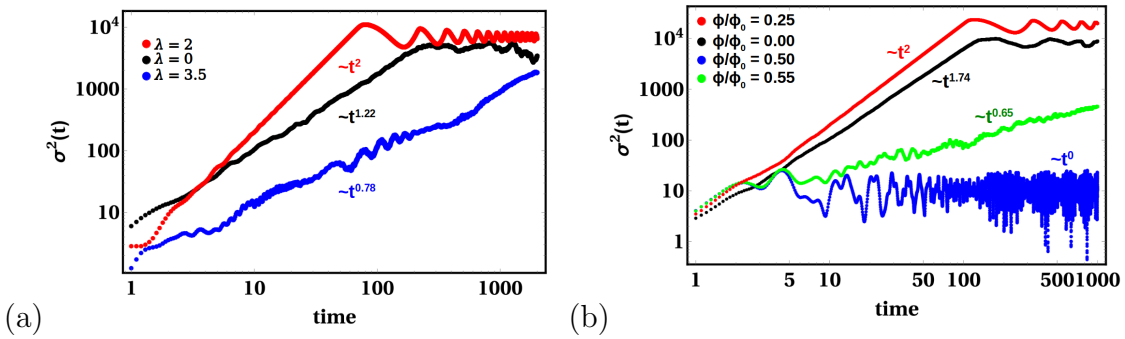

(a) (b)

Figure 8: (Color online) The mean-square displacement of a wave packet as a function of time (in a log-log scale) for the Fibonacci sequence of (a) 'dimer-stub' ($N = 290$ sites) with different values of the tunnel hopping amplitude λ, and (b) 'diamond-stub' ($N = 468$ sites) with different values of trapped magnetic flux. The parameters are chosen as (a) $\epsilon = 0$, $L = 1$, $S = \sqrt{5}$, $\lambda = 0$ (black colored), 2 (red colored), 3.5 (blue colored) and for (b) $\epsilon = 0$, $L = 1$, $\frac{\Phi}{\Phi_0} = 0$ (black colored), 0.25 (red colored), 0.50 (blue colored), 0.55 (green colored) respectively.

C_n denotes the initial ($t = 0$) probability amplitude of finding the particle found on the n^{th} site. If the particle is released at some m^{th} site, then $C_n(0) = \langle \psi_n(0) | m \rangle$. After some time, the time-evolved state is given by [25, 28],

$$|\Psi(t)\rangle = \sum_n C_n e^{-iE_n t} |\psi_n(0)\rangle \tag{25}$$

We now study the fundamental quantities that govern the quantum dynamics of a wave packet on finite-sized systems with the geometries shown in Fig. 7(a) and (b).

The mean square displacement (MSD) measures the spreading of the wave packet with time, which was initially at a particular site m (say) at $t = 0$. It is defined as [25],

$$\sigma^2(t) = \sum_n (n - m)^2 |\Psi_n(t)|^2 \tag{26}$$

The behaviour of $\sigma^2(t)$ displays an asymptotic dependence on time in the long time limit, and is described by a power law [25] form $\sigma^2(t) \sim t^\mu$. Depending upon the numerical values of this exponent μ, the dynamics of quantum wave packets can be classified as sub-diffusive for $0 < \mu < 1$, localized, for $\mu = 0$ [29, 30, 31], whereas $\mu = 1$, $2 > \mu > 1$, and $\mu = 2$ indicate ordinary diffusion, super diffusion, and ballistic motion respectively [25].

The variation of MSD with time in a Fibonacci array of the 'dimer-stub' quantum network is Shown in Fig. 8(a). Here we have chosen the hopping integral along the horizontal bonds on the backbone as $L = 1$, and $S = \sqrt{5}$. The tunnel hopping amplitude between the stub-atom (red) and the base atom (blue), denoted by λ, is varied. $\lambda = 2$ is our so called 'resonance' condition. At the resonance condition, the infinite system was shown to exhibit two absolutely continuous subbands, and we examine what happens to the long time dynamics when we have a finite sized system.

When $\lambda = 0$ the system boils down to a linear Fibonacci array of L and S with isolated uncoupled dots (red colored) on one side. The long time beahvior of the wave packet shows a power law $\sim t^{1.22}$, obtained using a best fit. The system behaves super diffusively. With $\lambda = 3.5$ the sub-diffusive behaviour sets in as the asymptotic (in time) behavior gives the best fit a power law $\sim t^{0.78}$. The long time behavior when the tunnel coupling $\lambda = 2$ is obtained using a best fit again, and the temporal behavior is found to be governed by a scaling law of $\sigma^2(t) \sim t^2$.

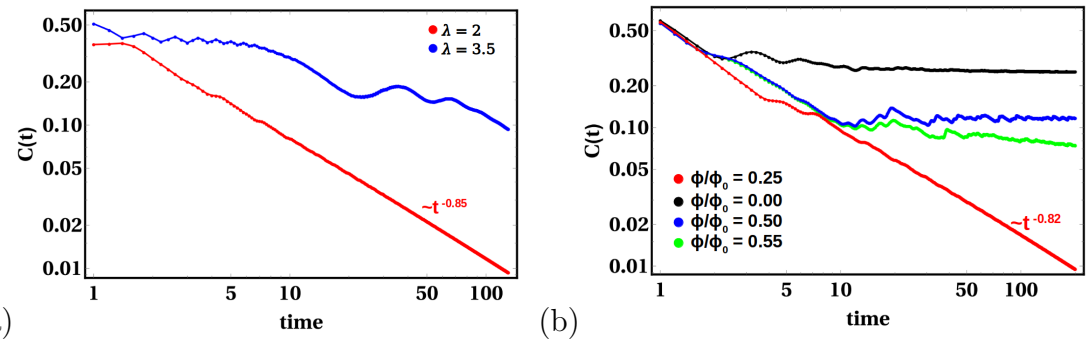

Figure 9: (Color online) The temporal auto-correlation function is plotted against time using a log-log scale, for the Fibonacci sequence of (a) 'dimer-stub' ($N = 290$ sites) with different values of the external hopping parameter λ and (b) 'diamond-stub' ($N = 468$ sites) with different values of applied magnetic flux. The parameters are chosen as (a) $\epsilon = 0$, $L = 1$, $S = \sqrt{5}$, $\lambda = 2$ (red colored), 3.5 (blue colored) and for (b) $\epsilon = 0$, $L = 1$, $\frac{\Phi}{\Phi_0} = 0$ (black colored), 0.25 (red colored), 0.50 (blue colored), 0.55 (green colored) respectively.

The MSD as a function of time for the 'diamond-stub' Fibonacci sequence is shown in Fig. 8(b). Now the magnetic flux trapped in each diamond-cavity, plays the all important role to control the wave packet dynamics. Without any flux the MSD with time shows, in the long time limit, a power law $\sim t^{1.74}$. The system is found to be in a super diffusive state. For an applied magnetic flux $\Phi = \frac{1}{4}\Phi_0$ in each diamond plaquette, the system achieves the resonance condition, and the scaling exponent μ is ≈ 2, corresponding to the ballistic motion. The time exponent μ is ≈ 0 when each diamond cavity is trapped by a magnetic flux $\Phi = \frac{1}{2}\Phi_0$. This is essentially an example of an *extreme localization* [32].

If a wave packet is initially released at a particular site m at time $t = 0$, then at a later time t the probability of finding the wave packet at site m is given by $P_m(t) = |\Psi_m(t)|^2$. This is the return probability (RP). After evolving for a long time if RP at the initial site m (and/or its neighborhood) is still finite, we get an indication of localization in general. For a delocalized phase, as the time flows on, the RP decays to zero [33].

The temporal autocorrelation function (TAF) is a time-averaged representation of the return probability [25, 28].

$$C(t) = \frac{1}{t}\int_0^t |\Psi_m(t)|^2\, dt \tag{27}$$

The behaviour of TAF for large times is dictated by the power-law [25] $C(t) = t^{-\delta}$. For a completely periodic system, this exponent δ is ≈ 1 in the long time limit.

In Fig. 9 (a) the TAF is plotted, in a log-log scale, against time for the 'dimer-stub' network and we find that, as we set $\lambda = 2$ (the resonance condition) the decay of $C(t)$ after a long time exhibits a power-law-like form $t^{-\delta}$ with the exponent δ taking up a value close to 0.85 when time is not so large. This is shown by the red line in Fig. 9 (a). Going to an even longer time, we have checked that the exponent comes even closer to unity. For $\lambda = 3.5$, a strong deviation from our resonance condition, the TAF has a very small decay-rate with time (blue colored line) which can be attributed again to the sub-diffusive character of the wave packet.

The variation of $C(t)$ with time for the Fibonacci sequence of 'diamond-stub' is shown in Fig. 9(b) when a constant magnetic flux is trapped in each diamond cavity. For $\Phi = \frac{1}{4}\Phi_0$ (resonance condition) after a large time it has a tendency to follow $C(t) \approx t^{-1}$ (red colored) whereas its decay for other values of the magnetic flux are depicted in the same figure shows the localized nature of the wave packet, a typical characteristic of the underlying quasiperiodic structure.

Information entropy (IE) is a very popular measurement to detect (de)localization [34]. This is written in the following form [25, 35, 36],

$$S(t) = -\sum_n P_n \log P_n \tag{28}$$

Where $P_n = |\Psi_n(t)|^2$ is the probability of finding the wave packet in its n^{th} state with $0 \leqslant P_n \leqslant 1$ and $\sum_n P_n = 1$. For a delocalized phase, the wave packet spreads throughout the lattice from its initial position m as time evolves. As a result, there is a finite probability of finding the wave packet on each site of the system. In the case of localization, the wave packet is still confined around its initial location m after a long time interval so that, very close to m the probability is high, and in all other positions the probability is almost zero. Due to this type of probability distribution $S(t)$ increases monotonically with time [25] when the system is delocalized, and a saturation appears when the wavepacket fully spreads all over the system. The value of the saturation-point increases linearly with the system size [36, 37] because, with an increasingly large system size, the wavepacket takes greater time to spread out. Hence, $S(t)$ shows a greater saturation value, and the saturation sets in at a later time. On the other hand, the IE shows a very short time growth followed by saturation in a localized phase, and this saturation is not affected by the system size [34, 38, 36]. Because, for the localized phase the wavepacket is always centered around its initial location (no spreading), no matter for how long the system evolves with time.

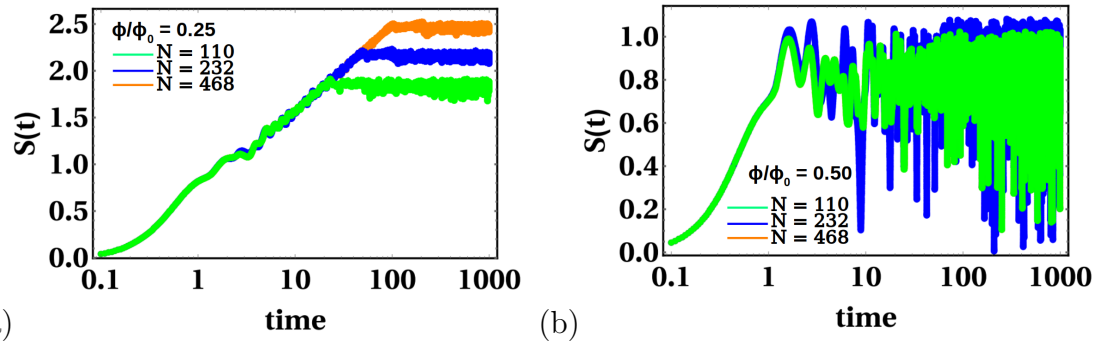

(a) (b)

Figure 10: (Color online) The information entropy is plotted against time (in a log scale) for a Fibonacci sequence of diamond-shaped network for different system size $N = 468$ (orange colored), $N = 232$ (blue colored) and $N = 110$ (green colored) with stubs when a uniform magnetic flux (Φ) (a) $\Phi = \frac{1}{4}\Phi_0$ and (b) $\Phi = \frac{1}{2}\Phi_0$ is trapped in each plaquette. The orange colored plot for $N = 468$ overlaps with the two other colors, and is not visible. The hopping integrals are chosen as $L = 1$ and all on-site potentials are set as zero. The initial site where the wavepacket is released is chosen as $m = 234^{th}$, $m = 114^{th}$ and $m = 56^{th}$ for system size $N = 468$, $N = 232$ and $N = 110$ respectively.

The information entropy versus time for a Fibonacci sequence of a 'diamond-stub' network is shown in Fig. 10 for different system sizes. At $\Phi = \frac{1}{4}\Phi_0$, the saturation of $S(t)$ increases in proportion with the size of system. It is apparent that before the saturation is in every case $S(t)$ has an almost monotonic increase in time. This again indicates that the wavepacket under the resonance condition of $\Phi = \frac{1}{4}\Phi_0$ exhibits a purely delocalized character (Fig. 10(a)). When each diamond plaquette is trapped by the magnetic flux $\Phi = \frac{1}{2}\Phi_0$, information entropy for different system sizes shows an overlapping of the saturation zone which is totally independent of system size (as shown in Fig. 10(b)) as a result. This is the pinned localized phase. The wavepacket gets *frozen*, and is localized within a very small spatial extent around the initial point of release.

As a final check over all our conclusions drawn so far, we investigate the nature of the inverse participation ratio (IPR) when the system evolves with time. The inverse participation ratio is defined as [39, 27],

$$IPR(t) = \sum_n |\Psi_n(t)|^4 \tag{29}$$

Here n is the atomic site index. At $t = 0$ the wavepacket is on its initial location m, such that only $|\Psi_m(t)|^4$ gives 1, and at all other locations n it is zero. As a result $IPR(0) = 1$.

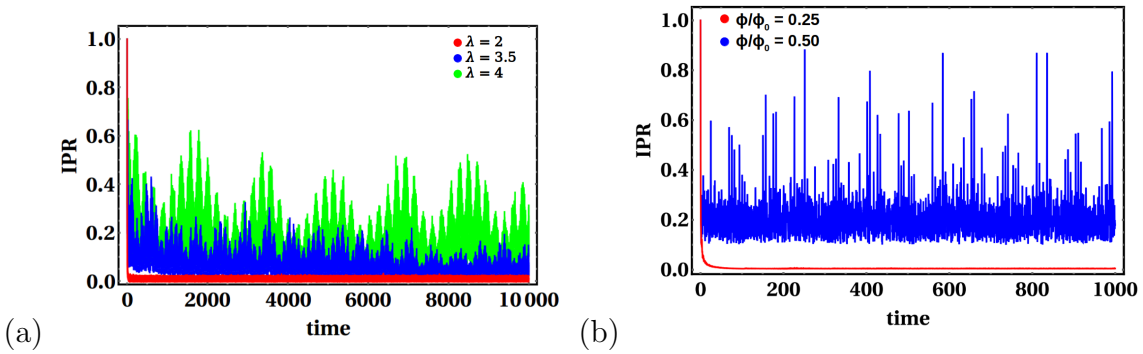

Figure 11: (Color online) The inverse participation ratio is plotted against time for the Fibonacci sequence of (a) 'dimer-stub' quantum network (290 sites) with different values of the external hopping parameter $\lambda = 2$ (red colored), 3.5 (blue colored), 4 (green colored) and (b) for 'diamond-stub' network (468 sites) with different values of applied magnetic field $\Phi = \frac{1}{4}\Phi_0$ (red colored), $\Phi = \frac{1}{2}\Phi_0$ (blue colored) respectively. Initially, we put the wave packet at the $141^{th}(234^{th})$ site for 'dimer-stub'('diamond-stub) systems respectively. The hopping integrals are chosen as (a) $L = 1$, $S = \sqrt{5}$, (b) $L = 1$, and all on-site potentials are set as zero.

The variation of inverse participation ratio with time for a Fibonacci sequence of 'dimer-stub' quantum network is shown in Fig. 11(a) when the external hopping amplitude λ is tuned. At resonance ($\lambda = 2$) the system is equivalent to a periodic one, and hence under time evolution, IPR(t) goes to zero (red colored). When $\lambda = 3.5$ or 4, the dynamics represent the sub-diffusive regime the IPR shows an oscillatory behaviour between some non-zero values, slowly dropping down to zero for a very long time, indicating an eventual escape of the wave packet.

A similar plot for the 'diamond-stub' Fibonacci sequence is shown in Fig. 11(b) when a uniform magnetic flux is trapped in each diamond cavity. When a constant flux $\Phi = \frac{1}{4}\Phi_0$ is applied, the resultant IPR drops to zero (red colored) with time, whereas a purely localized phase appears at $\Phi = \frac{1}{2}\Phi_0$ and IPR is always gives a non-zero value with an oscillatory character (blue colored lines).

2.4 Topological properties of a class of generalized Su-Schrieffer-Heeger networks: chains and meshes

Physica B 685 (2024) 416025

Contents lists available at ScienceDirect

Physica B: Condensed Matter

journal homepage: www.elsevier.com/locate/physb

Topological properties of a class of generalized Su–Schrieffer–Heeger networks: Chains and meshes

Sougata Biswas *, Arunava Chakrabarti

Department of Physics, Presidency University, 86/1 College Street, Kolkata, West Bengal, 700 073, India

In this part of the thesis we propose to inspect the topological properties of a class of generalized SSH chains (GSSHC), followed by an in-depth study of the band and topological aspects of a mesh designed out of such GSSHC's that crisscross each other forming a quasi-one-dimensional network. The network is infinitely extended along the x-direction and is finite, but arbitrarily wide along the y-direction. We call such a geometry a *generalized SSH mesh* (GSSHM). The constituent chains in the GSSHM are geometrically entangled, mimicking the situation in a polymeric system. In our work, both for the one-dimensional GSSHC family

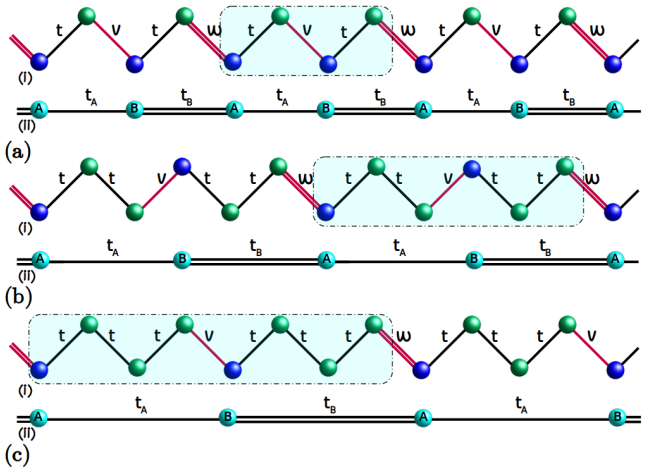

Figure 12: (Color online) (a)(i), (b)(i), and (c)(i) show three different types of generalized SSH chains (GSSHC), referred to in the text as GSSHC-I, GSSHC-II, and GSSHC-III respectively. Each GSSHC is built by arranging three different nearest neighbor hoppings, viz, t, v, and w in the orders shown. After decimating the green-colored sites, the GSSHC variants are transformed (renormalized) into chains with two different sublattices A and B, as shown in (a)(ii), (b)(ii) and (c)(ii) respectively. The unit cells are marked by the shaded box in each case.

and the GSSHM geometries, we include an *additional* overlap integral, marked by t in Fig. 12. The inclusion of such an extra hopping element *delays*, in space, the staggering (alternating) pattern of the two other hopping integrals, marked v and w, that are hallmarks of a traditional SSH chain. The effect of this third interaction, on the topological properties of the systems studied is not obvious, and we explore this area in some detail. We find that, even with a

delayed staggering effect caused by the presence of one or multiple 'extra' hopping integral (t) the bands in one-dimensional GSSH models show quantized topological invariant. The story of the quasi-one-dimensional GSSHM systems is not so trivial. There we need a threshold value of t beyond which the Zak phase becomes quantized, in contrast to their one-dimensional counterparts.

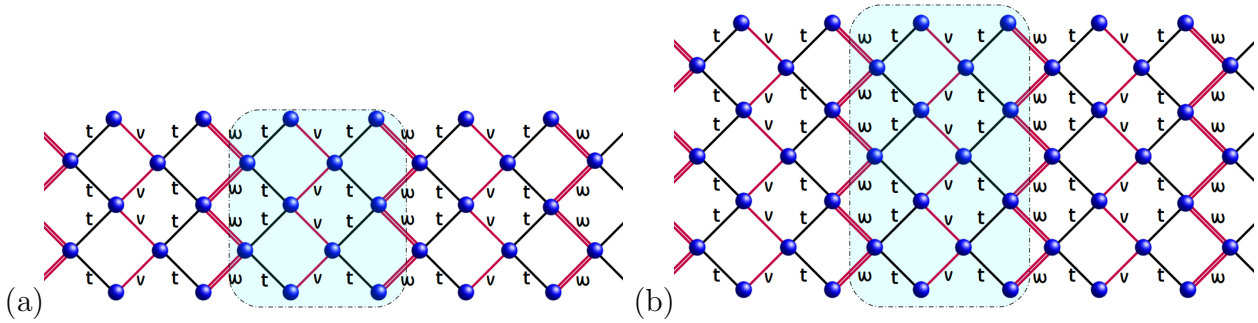

Figure 13: (Color online) Cross-linking of (a) four and (b) six GSSHC-I (as shown in Fig. 12 a(i)). The unit cells are marked by a cyan-shaded box.

In Fig. 12(a)(ii) one easily identifies two sublattices (A and B). The process of decimation renders the on-site potentials and the effective nearest neighbor hopping integrals on the *new* lattice energy dependent. These new, *renormalized* on-site potentials are named ϵ_A, ϵ_B respectively, and the new nearest neighbor hopping integrals are termed t_A, t_B, which alternate periodically. They are given by,

$$\begin{aligned} \epsilon_A &= \epsilon + \frac{w^2+t^2}{E-\epsilon} \\ \epsilon_B &= \epsilon + \frac{v^2+t^2}{E-\epsilon} \\ t_A &= \frac{vt}{E-\epsilon} \\ t_B &= \frac{wt}{E-\epsilon} \end{aligned} \tag{30}$$

A set of difference equations, written for this renormalized two-sublattice chain, given in Fig. 12(a)(ii), is easily written as,

$$\begin{aligned} (E-\epsilon_A)\psi_{j\subset A} &= t_B\psi_{j-1\subset B} + t_A\psi_{j+1\subset B} \\ (E-\epsilon_B)\psi_{j\subset B} &= t_A\psi_{j-1\subset A} + t_B\psi_{j+1\subset A} \end{aligned} \tag{31}$$

The above set of equations represents an effective SSH chain with on-site, energy-dependent potentials ϵ_A and ϵ_B, and periodically alternating 'hopping amplitudes' t_A and t_B. Keeping in mind the analysis of a traditional SSH chain it is easy to appreciate that the energy spectrum of this system will have band gaps closed at the Brillouin zone boundaries when $E-\epsilon_{A(B)}=0$, and $t_A=t_B$. This leads to,

$$\begin{aligned} E &= \epsilon \pm \sqrt{v^2+t^2} \\ v &= w \end{aligned} \tag{32}$$

To work out the dispersion relation in general, for any combination of v and w, we first simplify Eqs. (31) using Eqs. (30), to

$$\begin{aligned} [(E-\epsilon)^2-\beta]\psi_{j\subset A} &= wt\ \psi_{j-1\subset B} + vt\ \psi_{j+1\subset B} \\ [(E-\epsilon)^2-\alpha]\psi_{j\subset B} &= vt\ \psi_{j-1\subset A} + wt\ \psi_{j+1\subset A} \end{aligned} \tag{33}$$

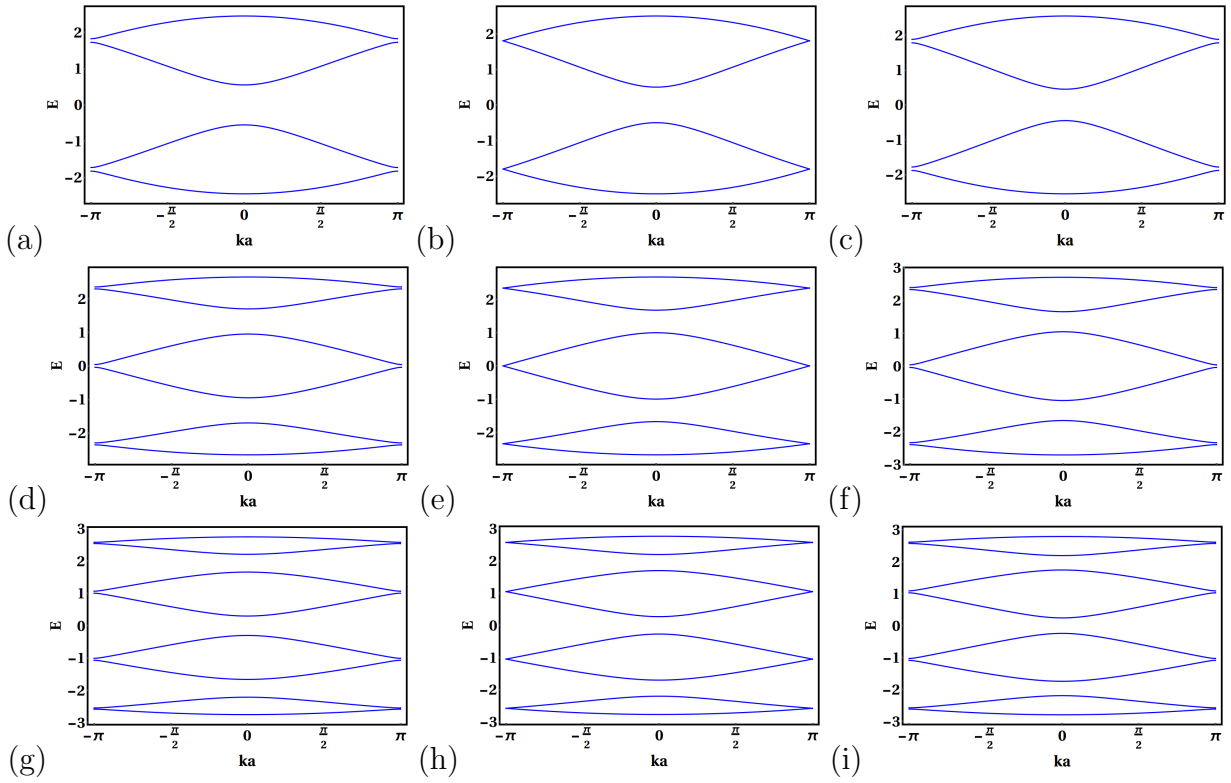

Figure 14: (Color online) Energy bands (a,b,c) for GSSHC-I (Fig. 12(a)), (d,e,f) for GSSHC-II (Fig. 12(b)) and (g,h,i) for GSSHC-III (Fig. 12(c)) respectively. We have chosen (a,d,g) $t = 1.5$, $\epsilon = 0$, $v = 1$, $w = 0.9$, (b,e,h) $t = 1.5$, $\epsilon = 0$, $v = 1$, $w = 1$ and (c,f,i) $t = 1.5$, $\epsilon = 0$, $v = 1$, $w = 1.1$. For both the cases $v > w$ and $v < w$ all these variants have a quantized Zak phase for all bands, as will be discussed later.

where, $\alpha = (v^2 + t^2)$ and $\beta = (w^2 + t^2)$. A further decimation of the alternate sites on this effective chain maps it to a simple 1-d perfectly periodic chain with a new onsite potential $\tilde{\epsilon}$ and a uniform hopping integral $\tilde{t}$, given by,

$$\begin{aligned} \tilde{\epsilon} &= \epsilon_A + \frac{{t_A}^2 + {t_B}^2}{E - \epsilon_B} \\ \tilde{t} &= \frac{t_A t_B}{E - \epsilon_B} \end{aligned} \tag{34}$$

It is now simple to work out the dispersion relations for the effective 1-d chains. The dispersion relation is written as,

$$E = \tilde{\epsilon} + 2\tilde{t}\cos\ ka' \tag{35}$$

Here, 'a'' represents the effective lattice spacing of the renormalized 1-d periodic chain and k is the wave vector. Using Eqs. (30), and Eqs. (34), the dispersion relation Eq. (35) of the effective 1-d period chain is expanded to obtain

$$(E - \epsilon)^4 - (E - \epsilon)^2(\beta + \alpha) + \alpha\beta - \gamma t^2 - 2vwt^2\cos\ ka' = 0 \tag{36}$$

where, $\alpha = (v^2 + t^2)$, $\beta = (w^2 + t^2)$ and $\gamma = (v^2 + w^2)$. All the dispersive bands of such a GSSHC-I type lattice are easily obtained from the solutions of the Eqs. (36).

We display the dispersive energy bands corresponding to the GSSHC-I chain in Fig. 14 (a), (b), and (c) for the three cases, $v > w$, $v = w$, and $v < w$ respectively. The bands are obtained by a direct diagonalization of the matrix written in k-space, corresponding to the

unit cell. The on-site potential is set at $\epsilon = 0$, and the hopping integral is chosen as $t = 1.5$. For $v = w = 1$, and $t = 1.5$ the gaps at the BZ boundaries are found to close exactly at $E = \pm\sqrt{v^2 + t^2} = \pm\sqrt{w^2 + t^2}$, as we expect from our earlier arguments. All the dispersive bands, obtained from an exact diagonalization, matches exactly the results obtained from the decimation scheme, including the magnitudes of the gap-closing energies.

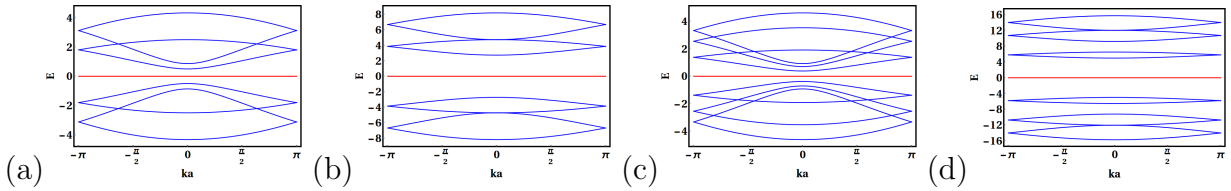

Figure 15: (Color online) Energy-wave vector (E vs. ka) dispersion relation (a,b) four cross-linked GSSHC-I (Fig. 13(a)) and (c,d) six cross-linked GSSHC-I(Fig. 13(b)) respectively. We have chosen (a,c) $t = 1.5$, $\epsilon = 0$, $v = 1$, $w = 1$, (b) $t = 3.73205$, $\epsilon = 0$, $v = 1$, $w = 1$ and (d) $t = 7.52395$, $\epsilon = 0$, $v = 1$, $w = 1$.

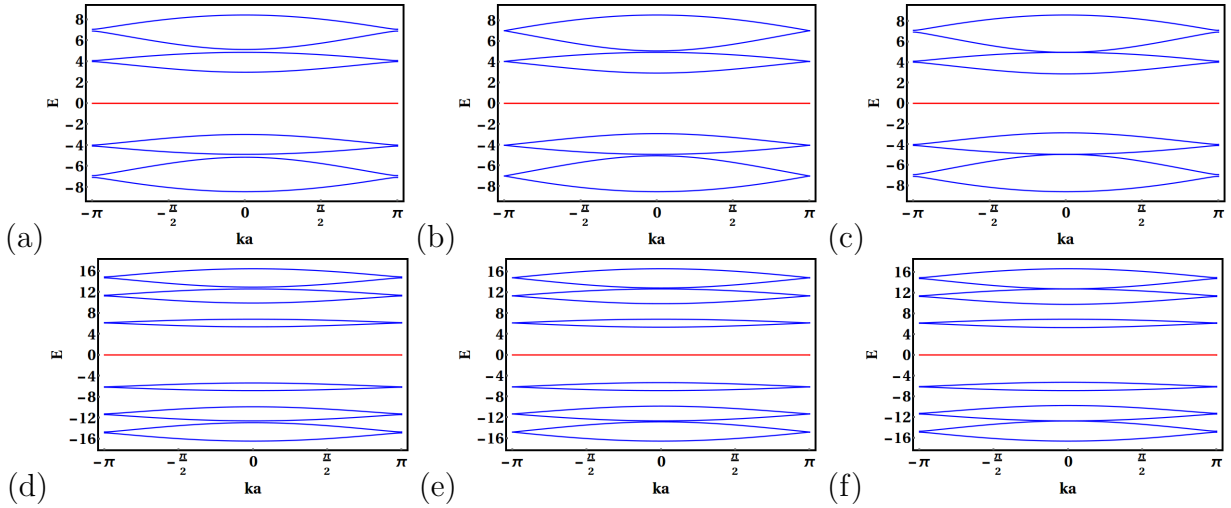

Figure 16: (Color online) Energy-wave vector (E vs. ka) dispersion relation (a,b,c) for cross-linking of four, (d,e,f) for cross-linking of six GSSHC-I respectively. We have chosen (a) $t = 3.92$, $\epsilon = 0$, $v = 1$, $w = 0.9$, (b) $t = 3.92$, $\epsilon = 0$, $v = 1$, $w = 1$, (c) $t = 3.92$, $\epsilon = 0$, $v = 1$, $w = 1.1$, (d) $t = 7.95$, $\epsilon = 0$, $v = 1$, $w = 0.9$, (e) $t = 7.95$, $\epsilon = 0$, $v = 1$, $w = 1$ and (f) $t = 7.95$, $\epsilon = 0$, $v = 1$, $w = 1.1$,. The flat bands (doubly degenerate) are marked in red. For both cases $v > w$ and $v < w$ all these networks have a quantized zak phase for all dispersive bands .

The kernels of the Hamiltonian ($\hat{\mathcal{H}}_1(k)$, $\hat{\mathcal{H}}_2(k)$, $\hat{\mathcal{H}}_3(k)$) for the unit cell of the GSSHC-I, GSSHC-II, GSSHC-III(as shown in Fig. 12) are given by,

$$\hat{\mathcal{H}}_1(k) = \begin{bmatrix} \epsilon & t & 0 & we^{-ika} \\ t & \epsilon & v & 0 \\ 0 & v & \epsilon & t \\ we^{ika} & 0 & t & \epsilon \end{bmatrix} \tag{37}$$

$$\hat{\mathcal{H}}_2(k) = \begin{bmatrix} \epsilon & t & 0 & 0 & 0 & we^{-ika} \\ t & \epsilon & t & 0 & 0 & 0 \\ 0 & t & \epsilon & v & 0 & 0 \\ 0 & 0 & v & \epsilon & t & 0 \\ 0 & 0 & 0 & t & \epsilon & t \\ we^{ika} & 0 & 0 & 0 & t & \epsilon \end{bmatrix} \tag{38}$$

$$\hat{\mathcal{H}}_3(k) = \begin{bmatrix} \epsilon & t & 0 & 0 & 0 & 0 & 0 & we^{-ika} \\ t & \epsilon & t & 0 & 0 & 0 & 0 & 0 \\ 0 & t & \epsilon & t & 0 & 0 & 0 & 0 \\ 0 & 0 & t & \epsilon & v & 0 & 0 & 0 \\ 0 & 0 & 0 & v & \epsilon & t & 0 & 0 \\ 0 & 0 & 0 & 0 & t & \epsilon & t & 0 \\ 0 & 0 & 0 & 0 & 0 & t & \epsilon & t \\ we^{ika} & 0 & 0 & 0 & 0 & 0 & t & \epsilon \end{bmatrix} \tag{39}$$

When Four and Six GSSHC-I are cross-linked (as shown in Fig. 13) then kernels of the Hamiltonian ($\hat{\mathcal{H}}_4(k)$, $\hat{\mathcal{H}}_5(k)$) become,

$$\hat{\mathcal{H}}_4(k) = \begin{bmatrix} \epsilon & 0 & 0 & t & t & 0 & 0 & 0 & we^{-ika} & we^{-ika} \\ 0 & \epsilon & t & t & 0 & 0 & 0 & we^{-ika} & we^{-ika} & 0 \\ 0 & t & \epsilon & 0 & 0 & v & 0 & 0 & 0 & 0 \\ t & t & 0 & \epsilon & 0 & v & v & 0 & 0 & 0 \\ t & 0 & 0 & 0 & \epsilon & 0 & v & 0 & 0 & 0 \\ 0 & 0 & v & v & 0 & \epsilon & 0 & t & t & 0 \\ 0 & 0 & 0 & v & v & 0 & \epsilon & 0 & t & t \\ 0 & we^{ika} & 0 & 0 & 0 & t & 0 & \epsilon & 0 & 0 \\ we^{ika} & we^{ika} & 0 & 0 & 0 & t & t & 0 & \epsilon & 0 \\ we^{ika} & 0 & 0 & 0 & 0 & 0 & t & 0 & 0 & \epsilon \end{bmatrix} \tag{40}$$

$$\hat{\mathcal{H}}_5(k) = \begin{bmatrix} \epsilon & 0 & 0 & 0 & 0 & t & t & 0 & 0 & 0 & 0 & 0 & we^{-ika} & we^{-ika} \\ 0 & \epsilon & 0 & 0 & t & t & 0 & 0 & 0 & 0 & 0 & we^{-ika} & we^{-ika} & 0 \\ 0 & 0 & \epsilon & t & t & 0 & 0 & 0 & 0 & 0 & we^{-ika} & we^{-ika} & 0 & 0 \\ 0 & 0 & t & \epsilon & 0 & 0 & 0 & v & 0 & 0 & 0 & 0 & 0 & 0 \\ 0 & t & t & 0 & \epsilon & 0 & 0 & v & v & 0 & 0 & 0 & 0 & 0 \\ t & t & 0 & 0 & 0 & \epsilon & 0 & 0 & v & v & 0 & 0 & 0 & 0 \\ t & 0 & 0 & 0 & 0 & 0 & \epsilon & 0 & 0 & v & 0 & 0 & 0 & 0 \\ 0 & 0 & 0 & v & v & 0 & 0 & \epsilon & 0 & 0 & t & t & 0 & 0 \\ 0 & 0 & 0 & 0 & v & v & 0 & 0 & \epsilon & 0 & 0 & t & t & 0 \\ 0 & 0 & 0 & 0 & 0 & v & v & 0 & 0 & \epsilon & 0 & 0 & t & t \\ 0 & 0 & we^{ika} & 0 & 0 & 0 & 0 & t & 0 & 0 & \epsilon & 0 & 0 & 0 \\ 0 & we^{ika} & we^{ika} & 0 & 0 & 0 & 0 & t & t & 0 & 0 & \epsilon & 0 & 0 \\ we^{ika} & we^{ika} & 0 & 0 & 0 & 0 & 0 & 0 & t & t & 0 & 0 & \epsilon & 0 \\ we^{ika} & 0 & 0 & 0 & 0 & 0 & 0 & 0 & 0 & t & 0 & 0 & 0 & \epsilon \end{bmatrix} \tag{41}$$

We have gone for an exact diagonalization of the Hamiltonian corresponding to every example cited in this work, and the dispersive and the flat bands thus obtained, are compared with the results obtained out of the decimation procedure. The match is exact.

We can now have a critical look at the role of the relative magnitudes of the hopping integrals in determining the topological invariants.

It is apparent that every Hamiltonian has three hopping integrals, viz. t, v, and w. Among these v and w are responsible for gap-closing (for $v = w$) or opening (for $v \neq w$) at the Brillouin zone boundary. For all these models extensive numerical search reveals that a Dirac cone appears at $k = 0$ depending on a specific relationship between t, v, and w. After evaluating the dispersion relations it is possible to work out the exact mathematical relationship between the hopping integrals t, v and w for which the Dirac cone appears at $k = 0$. The condition for the appearance of the Dirac cone turns out to be,

$$t \;=\; \pm\sqrt{v}\sqrt{w} \tag{42}$$

To observe a topological phase transition, we need a gapped system. This requires that the strength of the hopping integral t be set to any value except $\pm\sqrt{v}\sqrt{w}$ as shown in Eqs. (42). Once this is implemented, all the bands get separated from each other and each of them has a quantized value of the Zak phase. The system exhibits a topological phase transition. This is true for even higher-order mesh structures, such as the four and six GSSHC-I cross-linked mesh families, as shown in Fig. 13.

It is important to appreciate that, the external parameter t plays a very important role in separating the energy bands. There is a particular value of t, a 'threshold' (t_{th}), above which all dispersive bands separate out from each other. precisely at $t = t_{th}$ pairs of dispersive bands just touch each other (as shown in Fig. 15((b) and (d))) and just above it the band-overlap is totally absent. The numerical value of t_{th} of course, is sensitive to the number of chains forming a mesh, that is, the width of the mesh. We have analytically calculated this threshold value t_{th} in terms of two other variables v and w. The t_{th} for the cross-linking of four GSSHC-I lattices is,

$$t_{th} = \pm\frac{\sqrt{3v^2 + 8vw + 3w^2 + 2\sqrt{3}\sqrt{(v+w)^4}}}{\sqrt{2}} \tag{43}$$

Similarly, for cross-linking of six GSSHC-I, it becomes,

$$\begin{aligned} t_{th} &= \pm\sqrt{a + 2\sqrt{2}\sqrt{b} + \frac{1}{2}\sqrt{c + 8a^2 - 2d + \eta}} \\ \eta &= \frac{64a^3 - 32ad - 32e}{16\sqrt{2}\sqrt{b}} \end{aligned} \tag{44}$$

where, $a = 4v^2+9vw+4w^2, b = v^4+4v^3w+6v^2w^2+4vw^3+w^4, c = 4v^4-10v^2w^2+4w^4, d = 14v^4+80v^3w+135v^2w^2+80vw^3+14w^4$, and $e = 4v^6+10v^5w+10vw^5-8v^4w^2-8v^2w^4-29v^3w^3+4w^6$.

First, for all models, the lattice constant (a) and onsite potentials (ϵ) are chosen as unity and zero respectively, throughout the chains. The Hamiltonian $\hat{\mathcal{H}}_i(k)$ ($i = 1, 2...5$) exhibits time-reversal symmetry, viz, $\hat{\mathcal{H}}(-k)^* = \hat{\mathcal{H}}(k)$. All the GSSHC and cross-linked GSSHC also obey the chiral symmetry operation, viz,

$$\mathcal{C}_i{}^{-1}\; \hat{\mathcal{H}}_i(k)\; \mathcal{C}_i \;=\; -\hat{\mathcal{H}}_i(k) \tag{45}$$

with $i = 1, 2..., 5$. The kernels of the Hamiltonians are already discussed, and the corresponding chiral operators ($\mathcal{C}_i$) are defined by,

$$
\begin{aligned}
\mathcal{C}_1 &= diag[1,-1,1,-1] \\
\mathcal{C}_2 &= diag[1,-1,1,-1,1,-1] \\
\mathcal{C}_3 &= diag[1,-1,1,-1,1,-1,1,-1] \\
\mathcal{C}_4 &= diag[1,1,-1,-1,-1,1,1,-1,-1,-1] \\
\mathcal{C}_5 &= diag[1,1,1,-1,-1,-1,-1,1,1,1,-1,-1,-1,-1]
\end{aligned}
\tag{46}
$$

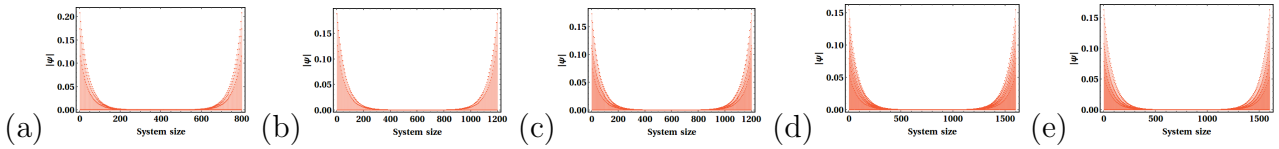

Figure 17: (Color online) Wave function distributions of the edge states (a) for GSSHC-I (Fig. 12(a)) with energies $E = \pm 1.80278$, (b,c) for GSSHC-II (Fig. 12(b)) with energies (b) $E = 0$, (c) $E = \pm 2.34521$, (d,e) for GSSHC-III (Fig. 12(c)) with energies (d) $E = \pm 2.57885$, (e) $E = \pm 1.04859$, respectively. All of these energies are doubly degenerate. We have used open boundary conditions for $N_x = 200$, where N_x denotes the number of unit cells taken along the x-direction. The values of the parameters are chosen as $t = 1.5$, $\epsilon = 0$, $v = 1$, $w = 1.1$ for all networks..

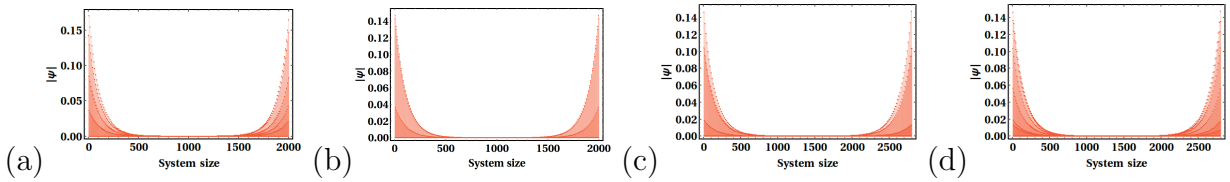

Figure 18: (Color online) Wave function distributions of the edge states (a,b) for cross-linking of four GSSHC-I(Fig. 13(a)) with energies (a)$E = \pm 7.00708$, (b) $E = \pm 4.04554$, and (c,d) for cross-linking of six GSSHC-I (Fig. 13(b)) with energies (c) $E = \pm 11.3316$, (d) $E = \pm 14.8054, E = \pm 6.13261$, respectively. All of these energies are doubly degenerate. We have used open boundary conditions for $N_x = 200$, where N_x denotes the number of unit cells taken along the x-direction. The values of the parameters are chosen as (a,b) $t = 3.92$, $\epsilon = 0$, $v = 1$, $w = 1.1$, and (c,d) $t = 7.95$, $\epsilon = 0$, $v = 1$, $w = 1.1$.

The Zak phase for the n-th bulk bands is defined as,

$$
Z = -i \oint_{BZ} \mathcal{A}_{nk}(k) dk \tag{47}
$$

where $\mathcal{A}_{nk}$ is called the Berry curvature of the n-th Bloch eigenstate.

The integral is done along a closed loop in the Brillouin zone. $|\psi_{nk}\rangle$ is the n-th Bloch state.The Zak phase is totally a bulk property of the system. To calculate the Zak phase of the bands, we use the Wilson loop approach [40, 41], by converting the integration Eqs. (47) into a summation over the Brillouin zone. It is a gauge invariant formalism. It protects the numerical value of the Zak phase against any arbitrary phase change of Bloch wavefunction. This summation for non-degenerate s-th band [40, 41] is given by Eqs. (48)

$$
Z_s = -Im \left[\log \prod_{k_n} \langle \psi_{k_n,s} | \, | \psi_{k_{n+1},s} \rangle \right] \tag{48}
$$

We calculate the Zak phase of all non-degenerate dispersive bands using Eqs. (48) for each GSSHC and two cross-linked GSSHC. The Zak phase always turns out to be quantized (either 0 or π) for any value of the external parameter t. Still, the $t = \pm\sqrt{v}\sqrt{w}$ situation must be avoided due to the formation of the Dirac cone at $k = 0$.

The calculation of the Zak phase of multiple cross-linked GSSHC gives quantized values (either 0 or pi) for the dispersive bands which have no overlap in between them. For bands that do overlap, the Zak phase can not be defined. The separation of such bands is, as stated earlier, engineered by choosing t appropriately.

To see the edge states we construct a finite-sized GSSHC and cross-linked GSSHC just by joining two hundred unit cells in the x direction. The values of the edge state energies are found to be the same (for all practical purposes) to the 'gap-closing' energies. On the other hand, when $v > w$, no gap-states are observed in the energy spectra at these edge-state energies. The behavior of edge states is shown in Fig. 17 and Fig. 18, which indicates an absence of any state in the bulk portion of these GSSHC and cross-linked GSSHC systems.

In conclusion, we have studied a large family of cross-linked generalized SSH chains, forming a mesh. The width of the mesh may vary from a trivial two-chain limit to an arbitrarily large value. We find that one particular parameter, namely a hopping integral (t here) that punctuates the usual SSH kind of staggering between the two others (v and w) plays a crucial role in making the mesh topologically non-trivial.

3 Acknowledgement

I would like to express my sincere gratitude to my supervisor Prof. Arunava Chakrabarti for his guidance and invaluable advice. I am really grateful to Prof. Muktish Acharyya for his fruitful suggestions and illuminating discussions. I am thankful to the Government of West Bengal for the SVMCM Scholarship (WBP221657867058).

4 List of Research Works

- "Designer quantum states on a fractal substrate: compact localization, flat bands and edge mode", Sougata Biswas and Arunava Chakrabarti, Physica E 153 (2023), 115762
- "Complete escape from localization on a hierarchical lattice: A Koch fractal with all states extended", Sougata Biswas and Arunava Chakrabarti, Physical Review B 108, 125430 (2023)
- "Engineering complete delocalization of single particle states in a class of one dimensional aperiodic lattices: a quantum dynamical study", Sougata Biswas, Arunava Chakrabarti, Physica E 162 (2024) 116010
- "Topological properties of a class of generalized Su–Schrieffer–Heeger networks: Chains and meshes", Sougata Biswas and Arunava Chakrabarti, Physica B 685 (2024) 416025
- "Flat bands and topological phase transition in entangled Su-Schrieffer -Heeger chains", Sauvik Chatterjee, Sougata Biswas, and Arunava Chakrabarti, arXiv:2304.00904, (Accepted for publication in International Journal of Modern Physics B)
- "Flat bands, edge states and possible topological phases in a branching fractal", Sougata Biswas, Amrita Mukherjee, Arunava Chakrabarti, arXiv:2209.05117

5 Conferences Participated

- Presentation entitled "Designer quantum states on a fractal substrate: compact localization, flat bands and edge mode", at the Condensed Matter, Materials Science and Statistical Mechanics Symposium 2023, Presidency University, Kolkata.
- Presentation entitled "Entangled Su-Schrieffer-Heeger Chains: Flat Bands and Topological Issues", at the National Level Seminar on Recent Trends in Physics 2023, Acharya Prafulla Chandra College, Kolkata.
- Presentation entitled "Complete escape from localization on a hierarchical lattice: a Koch fractal with all states extended", at 3rd National Physics Meet, University of Kalyani, West Bengal 741235.

References

[1] I. Bloch, J. Dalibard, and J. Nsimbne, Quantum simulations with ultracold quantum gases, Nat. Phys. **8**, 267 (2012).

[2] R. Blatt and C. F. Roos, Quantum simulation with trapped ions, Nat. Phys. **8**, 277 (2012).

[3] R. A. Vicencio and C. Mejía-Cortés, J. Opt. 16, 015706 (2014).

[4] S. Rojas-Rojas, L. Morales-Inostroza, R. A. Vicencio, and A. Delgado, Phys. Rev. A 96, 043803 (2017).

[5] S. Xia, Y. Hu, D. Song, Y. Zong, L. Tang, and Z. Chen, "Demonstration of flat- band image transmission in optically induced Lieb photonic lattices,"Opt. Lett. **41**, 1435 (2016).

[6] A. Chakrabarti, Exact results for infinite and finite Sierpinski gasket fractals: extended electron states and transmission properties, J. Phys.: Condens. Matt. **8**, 10951 (1996). DOI 10.1088/0953-8984/8/50/021

[7] D. H. Dunlap, H-L. Wu, and Philip W. Phillips, Absence of localization in a random-dimer model, Phys. Rev. Lett. **65**, 88 (1990).

[8] H.-L. Wu and Philip Phillips, 194 citations Polyaniline is a random-dimer model: A new transport mechanism for conducting polymers, Phys. Rev. Lett. **66**, 1366 (1991).

[9] H.-L. Wu, William Goff, and Philip PhillipsInsulator-metal transitions in random lattices containing symmetrical defects, Phys. Rev. B **45**, 1623 (1992).

[10] P. K. Datta, D. Giri, and K. Kundu, Nonscattered states in a random-dimer model, Phys. Rev. B **47**, 10727 (1993).

[11] Angel Sánchez, Enrique Maciá, and Francisco Domínguez-Adame, Suppression of localization in Kronig-Penney models with correlated disorder, Phys. Rev. B **49**, 147 (1994).

[12] J. Heinrichs, Localization, antilocalization, and delocalization in one-dimensional disordered lattices, Phys. Rev. B **51**, 5699 (1995).

[13] R. Farchioni and G. Grosso, Electronic transport for random dimer-trimer model Hamiltonians, Phys. Rev. B **56**, 1170 (1997).

[14] S. Sil, S. N. Karmakar, R. K. Moitra, and A. Chakrabarti, Extended states in one-dimensional lattices: Application to the quasiperiodic copper-mean chain, Phys. Rev. B **48**, 4192(R) (1993).

[15] A. Chakrabarti, S. N. Karmakar, and R. K. Moitra, Renormalization-group analysis of extended electronic states in one-dimensional quasiperiodic lattices, Phys. Rev. B **50**, 13276 (1994).

[16] A. Chakrabarti, S. N. Karmakar, and R. K. Moitra, Role of a New Type of Correlated Disorder in Extended Electronic States in the Thue-Morse Lattice, Phys. Rev. Lett. **74**, 1403 (1995).

[17] E. Maciá and F. Domínguez-Adame, Physical Nature of Critical Wave Functions in Fibonacci Systems, Phys. Rev. Lett. **76**, 2957 (1996).

[18] A. Chakrabarti and B. Bhattacharyya, Atypical extended electronic states in an infinite Vicsek fractal: An exact result, Phys. Rev. B **54**, R12625(R) (1996).

[19] X. R. Wang, Phys. Rev. B **51**, 9310 (1995).

[20] A. Chakrabarti, Exact results for infinite and finite Sierpinski gasket fractals: extended electron states and transmission properties, J. Phys.: Condens. Matter **8**, 10951 (1996).

[21] A. Chakrabarti, Extended electron states and magnetotransport in a 3-simplex fractal, Phys. Rev. B **72**, 134207 (2005).

[22] A. Chakrabarti, Field induced delocalization in a Koch fractal, Phys. Rev. B **60**, 10576 (1999).

[23] Decimation means, eliminating the amplitudes ψ_j corresponding to the vertices A throughout the lattice in terms of the amplitudes at the sites B, C and D. This is done by using the difference equation.

[24] B. W. Southern, A. A. Kumar, P. D. Loly, and A.-M. S. Tremblay, Real-space rescaling method for the spectral properties of tight-binding systems, Phys. Rev. B **27**, 1405(R) (1983).

[25] D. E. Katsanos, S. N. Evangelou, and S. J. Xiong, Quantum electron dynamics in periodic and aperiodic sequences, Phys. Rev. B **51**, 895 (1995).

[26] F. S. Lozano-Negro, E. Alvarez Navarro, N. C. Chávez, F. Mattiotti, F. Borgonovi, H. M. Pastawski, and G. L. Celardo, Universal stability of coherently diffusive 1D systems with respect to decoherence, https://doi.org/10.48550/arXiv.2307.05656.

[27] F. S. Lozano-Negro, P. R. Zangara, H. M. Pastawski, Ergodicity breaking in an incommensurate system observed by OTOCs and loschmidt echoes: From quantum diffusion to sub- diffusion, Chaos, Solitons and Fractals, **150**, 111175 (2021).

[28] A. Maity and A. Chakrabarti, Engineering insulator-metal transition in a class of decorated lattices: a quantum dynamical study, Phys. Lett. A **406**, 127452 (2021).

[29] P. Siegle, I. Goychuk, and P. Hänggi, Origin of Hyperdiffusion in Generalised Brownian Motion, Phys. Rev. Lett **105** 100602 (2010).

[30] Jürgen Vollmer, Lamberto Rondoni, Muhammad Tayyab, Claudio Giberti, and Carlos Mejía-Monasterio, Displacement autocorrelation functions for strong anomalous diffusion: A scaling form, universal behavior, and corrections to scaling, Phys. Rev. Research **3**, 013067 (2021).

[31] Anna Bodrova, Awadhesh Kumar Dubey, Sanjay Puri, and Nikolai Brilliantov, Intermediate Regimes in Granular Brownian Motion: Superdiffusion and Subdiffusion, Phys. Rev. Lett. **109**, 178001 (2012).

[32] Julien Vidal, Rémy Mosseri, and Benoit Douçot, Aharonov-Bohm Cages in Two-Dimensional Structures, Phys. Rev. Lett. **81**, 5888 (1998).

[33] Chenguang Guan and Xingyue Guan,"A brief introduction to Anderson Localization", https://api.semanticscholar.org/CorpusID:211195988 (2019).

[34] Ravi Kumar and Ranjan Modak, Phys. Rev. B **105**, 224202 (2022).

[35] O. Farzadian, T. Oikonomou, M.R.R. Good, M.D. Niry, " Entropic analysis of the localization–delocalization transition in a one-dimensional correlated lattice", Physica A, vol **545**, 123350 (2020).

[36] Michele Coppola, Emanuele Tirrito, Dragi Karevski, Mario Collura, "Growth of entanglement entropy under local projective measurements", Phys. Rev. B **105**, 094303 (2022)

[37] Nakagawa, Y.O., Watanabe, M., Fujita, H. et al. "Universality in volume-law entanglement of scrambled pure quantum states". Nat Commun **9**, 1635 (2018).

[38] J. H. Bardarson, F. Pollmann, and J. E. Moore, Phys. Rev. Lett. **109**, 017202 (2012).

[39] Mauro Schiulaz, E. Jonathan Torres-Herrera, Francisco Pérez-Bernal, and Lea F. Santos, Phys. Rev. B **101**, 174312 (2020).

[40] T. Fukui, Y. Hatsugai, and H. Suzuki, Chern Numbers in Discretized Brillouin Zone, J. Phys. Soc. Jpn. **74**, 1674 (2005).

[41] Hai-Xiao Wang, Guang-Yu Guo, and Jian-Hua Jiang, Band topology in classical waves: Wilson-loop approach to topological numbers and fragile topology, New Jour. of Phys., **21**, (2019).

Arunava Chakrabarti

14.11.2024

Professor and Head
Department of Physics
Presidency University, Kolkata